Monthly Notices of the ROYAL ASTRONOMICAL SOCIETY

Mon. Not. R. Astron. Soc. **422,** 1294–1305 (2012) doi:10.1111/j.1365-2966.2012.20694.x

Discovery of the millisecond pulsar PSR J2043+1711 in a *Fermi* source with the Nançay Radio Telescope

L. Guillemot,[1★] P. C. C. Freire,[1★] I. Cognard,[2★] T. J. Johnson,[3,4] Y. Takahashi,[5] J. Kataoka,[5] G. Desvignes,[1] F. Camilo,[6] E. C. Ferrara,[7] A. K. Harding,[7] G. H. Janssen,[8] M. Keith,[9] M. Kerr,[10] M. Kramer,[1,8] D. Parent[4,11] S. M. Ransom,[12] P. S. Ray,[13] P. M. Saz Parkinson,[14] D. A. Smith,[15] B. W. Stappers[8] and G. Theureau[2]

[1]*Max-Planck-Institut für Radioastronomie, Auf dem Hügel 69, 53121 Bonn, Germany*
[2]*Laboratoire de Physique et Chimie de l'Environnement, LPCE UMR 6115 CNRS, F-45071 Orléans Cedex 02, and Station de radioastronomie de Nançay, Observatoire de Paris, CNRS/INSU, F-18330 Nançay, France*
[3]*National Research Council Research Associate, National Academy of Sciences, Washington, DC 20001, USA*
[4]*Naval Research Laboratory, Washington, DC 20375, USA*
[5]*Research Institute for Science and Engineering, Waseda University, 3-4-1, Okubo, Shinjuku, Tokyo 169-8555, Japan*
[6]*Columbia Astrophysics Laboratory, Columbia University, New York, NY 10027, USA*
[7]*NASA Goddard Space Flight Center, Greenbelt, MD 20771, USA*
[8]*Jodrell Bank Centre for Astrophysics, School of Physics and Astronomy, The University of Manchester, Manchester M13 9PL*
[9]*CSIRO Astronomy and Space Science, Australia Telescope National Facility, Epping, NSW 1710, Australia*
[10]*W. W. Hansen Experimental Physics Laboratory, Kavli Institute for Particle Astrophysics and Cosmology, Department of Physics and SLAC National Accelerator Laboratory, Stanford University, Stanford, CA 94305, USA*
[11]*Center for Earth Observing and Space Research, College of Science, George Mason University, Fairfax, VA 22030, USA*
[12]*National Radio Astronomy Observatory (NRAO), Charlottesville, VA 22903, USA*
[13]*Space Science Division, Naval Research Laboratory, Washington, DC 20375-5352, USA*
[14]*Santa Cruz Institute for Particle Physics, Department of Physics and Department of Astronomy and Astrophysics, University of California, Santa Cruz, CA 95064, USA*
[15]*Université Bordeaux 1, CNRS/IN2p3, Centre d'Études Nucléaires de Bordeaux Gradignan, 33175 Gradignan, France*

Accepted 2012 February 6. Received 2012 February 2; in original form 2011 November 25

ABSTRACT

We report the discovery of the millisecond pulsar PSR J2043+1711 in a search of a *Fermi* Large Area Telescope (LAT) source with no known associations, with the Nançay Radio Telescope. The new pulsar, confirmed with the Green Bank Telescope, has a spin period of 2.38 ms, is relatively nearby ($d \lesssim 2$ kpc) and is in a 1.48-d orbit around a low-mass companion, probably an He-type white dwarf. Using an ephemeris based on Arecibo, Nançay and Westerbork timing measurements, pulsed gamma-ray emission was detected in the data recorded by the *Fermi* LAT. The gamma-ray light curve and spectral properties are typical of other gamma-ray millisecond pulsars seen with *Fermi*. X-ray observations of the pulsar with *Suzaku* and the *Swift* X-ray Telescope yielded no detection. At 1.4 GHz, we observe strong flux density variations because of interstellar diffractive scintillation; however, a sharp peak can be observed at this frequency during bright scintillation states. At 327 MHz, the pulsar is detected with a much higher signal-to-noise ratio and its flux density is far more steady. However, at that frequency the Arecibo instrumentation cannot yet fully resolve the pulse profile. Despite that, our pulse time-of-arrival measurements have a post-fit residual rms of 2 μs. This and the expected stability of this system have made PSR J2043+1711 one of the first new *Fermi*-selected millisecond pulsars to be added to pulsar gravitational wave timing arrays. It has also allowed a significant measurement of relativistic delays in the times of arrival of the pulses due to the curvature of space–time near the companion, but not yet with enough

★E-mail: guillemo@mpifr-bonn.mpg.de (LG); pfreire@mpifr-bonn.mpg.de (PCCF); icognard@cnrs-orleans.fr (IC)

© 2012 The Authors
Monthly Notices of the Royal Astronomical Society © 2012 RAS

Downloaded from http://mnras.oxfordjournals.org/ at NASA Goddard Space Flight Ctr on July 14, 2014

precision to derive useful masses for the pulsar and the companion. Nevertheless, a mass for the pulsar between 1.7 and 2.0 $M_\odot$ can be derived if a standard millisecond pulsar formation model is assumed. In this paper, we also present a comprehensive summary of pulsar searches in *Fermi* LAT sources with the Nançay Radio Telescope to date.

Key words: pulsars: general – pulsars: individual: PSR J2043+1711 – gamma-rays: general.

1 INTRODUCTION

Searches for radio pulsars coincident with *Fermi* Large Area Telescope (LAT) gamma-ray sources with no known associations have been remarkably successful, with the discovery of more than 30 millisecond pulsars (MSPs) up to now (e.g. Cognard et al. 2011; Keith et al. 2011; Ransom et al. 2011). In addition, pulsed gamma-ray emission has been observed for about 20 previously known radio MSPs (Abdo et al. 2009, 2010b; Freire et al. 2011a; Guillemot et al. 2012). Finally, the LAT has observed gamma-ray emission from globular clusters with properties that are consistent with collective emission from populations of MSPs (Abdo et al. 2010d; Kong, Hui & Cheng 2010). MSPs are therefore an important class of gamma-ray sources.

MSPs are rapidly rotating neutron stars, characterized by small rotational periods ($P \lesssim 30$ ms) and period derivatives ($\dot{P} \lesssim 10^{-17}$). These pulsars are thought to be 'recycled', spun-up to millisecond periods by the accretion of matter and thus transfer of angular momentum from a binary companion (Bisnovatyi-Kogan & Komberg 1974; Alpar et al. 1982). More than 80 per cent of them are in binary systems, which makes searches for MSPs less sensitive than for normal pulsars. In addition, the MSPs discovered in *Fermi* LAT unassociated sources are widely distributed in Galactic latitude, whereas most radio pulsar surveys have concentrated on the Galactic plane. With its unprecedented sensitivity and localization accuracy (see Atwood et al. 2009), the LAT directs radio telescopes to high-latitude unassociated sources that could be unknown pulsars, missed by previous radio surveys. Moreover, positional uncertainties in the *Fermi* LAT Second Source Catalog (2FGL; Abdo et al. 2012) are comparable to typical radio beam sizes, making radio pulsation searches very efficient.

Despite the numerous discoveries, 30 per cent of the sources in the 2FGL catalogue remain unassociated and could potentially hide unknown gamma-ray pulsars. Pulsars seen by the *Fermi* LAT are characterized by gamma-ray spectra with sharp cut-offs at a few GeV and low flux variability (Abdo et al. 2009, 2010c). Observations of *Fermi* LAT unassociated sources from the First Source Catalog (1FGL; Abdo et al. 2010a) with curved spectra at the Nançay Radio Telescope (NRT) have previously yielded the discovery of two radio and gamma-ray MSPs, PSR J2017+0603 and PSR J2302+4442 (Cognard et al. 2011). In this paper, we describe a third NRT discovery, PSR J2043+1711, an MSP in a binary system located at the position of a *Fermi* LAT source with pulsar-like properties and no previously known, plausible associations.

This paper is organized as follows. In Sections 2.1 and 2.2, we describe the radio observations of PSR J2043+1711. In Section 2.3, we discuss the timing analysis of this MSP using the radio and the LAT data. In Sections 2.4 and 2.5, we describe the analysis of *Fermi* LAT data for the MSP, observed to emit pulsed gamma-rays, and the results of *Suzaku* observations yielding no detection of X-ray emission from the pulsar. In Section 3, we discuss some of the scientific results, including the modelling of the observed radio and gamma-ray light curves of PSR J2043+1711 in the context of theoretical models of emission in the outer magnetosphere of pulsars, and the detection of the Shapiro delay induced by the companion star at superior conjunction, which allowed us to place constraints on the neutron star mass (Section 3.2), and the detection of the proper motion and consequent limits on the distance to the pulsar (Section 3.3). Furthermore, in Section 3.3 we use the measured gamma-ray energy density to derive tighter upper limits for the distance. Once a precise distance is measured, these can be used to derive a lower limit for the moment of inertia of the star. We present a final summary and discuss some scientific prospects in Section 4.

2 OBSERVATIONS AND DATA ANALYSIS

2.1 Discovery observations

The *Fermi* LAT catalogue source 2FGL J2043.2+1711 was already listed in the 1FGL as 1FGL J2043.2+1709. It has no known counterpart, and has spectral and variability properties that made it a plausible gamma-ray pulsar, with a curvature index of 12.0 and a variability index of 12.2 in the 1FGL catalogue (see Abdo et al. 2010a, for definitions of the curvature and variability indices). A curvature index larger than 11.34 indicates that the source has a spectrum which departs from a pure power law at the 99 per cent confidence level, while a variability index larger than 23.21 implies that the source shows evidence of flux variability at the 99 per cent confidence level. With its lack of known associations, its gamma-ray properties that are reminiscent of those of known pulsars and high Galactic latitude ($b = -15\overset{\circ}{.}29$), 1FGL J2043.2+1709 satisfied all the criteria used for selecting the sources eligible for the original search for pulsars in *Fermi* LAT unassociated sources at Nançay that led to the discovery of PSR J2017+0603 and PSR J2302+4442 (Cognard et al. 2011), except for the spatial localization: the semi-major axis of the 1FGL source 95 per cent confidence ellipse (θ_{95}) was larger than the conservative cut of 3 arcmin used for the later search in order for sources to be well covered by the Nançay beam, which has a width at half-maximum of 4 arcmin in right ascension and 22 arcmin in declination. With additional data, the source localization improved ($\theta_{95} = 2.9$ arcmin in the 2FGL catalogue), making 2FGL J2043.2+1711 an excellent candidate source for radio pulsar searches with the NRT.[1]

A first 1-h observation of the source was made on 2009 November 21 at the NRT, using the modified Berkeley-Orléans-Nançay instrumentation (Cognard & Theureau 2006) at 1.4 GHz, with a 512 × 0.25 MHz incoherent filter bank sampled every 32 μs. The data were dedispersed in ∼2000 dispersion measure (DM) values, up to 1244 pc cm^{-3}, and processed using acceleration and single-pulse search techniques as provided by the PRESTO package (Ransom, Eikenberry & Middleditch 2002). No pulsations were observed in this initial observation. Similarly, the analysis of a second observation taken on 2009 December 2 yielded no detection.

[1] In addition to the successful search strategy just described, a number of other NRT observations of other *Fermi* LAT sources are documented in Appendix A.

© 2012 The Authors, MNRAS **422,** 1294–1305
Monthly Notices of the Royal Astronomical Society © 2012 RAS

Downloaded from http://mnras.oxfordjournals.org/ at NASA Goddard Space Flight Ctr on July 14, 2014

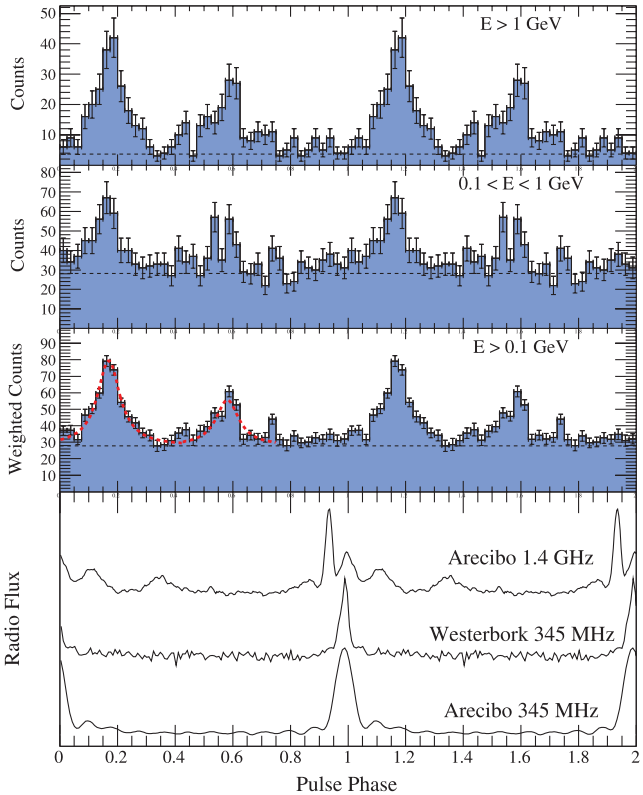

Figure 1. Multiwavelength light curves of PSR J2043+1711. The bottom panel shows radio profiles recorded at the Arecibo telescope at 345 MHz (40-min integration), at the WSRT at 345 MHz (3.8-h integration) and at the Arecibo telescope at 1.4 GHz (1-h integration). The third panel shows a 40-bin gamma-ray profile obtained by selecting events recorded by the *Fermi* LAT within 5° from the pulsar and with energies above 0.1 GeV, and weighting each event by its probability of originating from the pulsar. The fitting functions are shown as dashed lines in the first cycle. The top two panels show non-weighted *Fermi* LAT light curves for events recorded within 0.°8 of the pulsar, with energies between 0.1 and 1 GeV, and above 1 GeV, respectively. No gamma-ray features significantly narrower than the bin width used here were observed. Horizontal dashed lines indicate gamma-ray background levels. Two rotations are shown for clarity.

Nevertheless, a 19σ candidate with a rotational period of 2.379 ms and a DM of 20.7 pc cm^{-3} was observed in the third observation, taken on 2009 December 12. Seven subsequent observations of the *Fermi* LAT source at 1.4 GHz with the NRT yielded no redetection, casting doubts on the presence of a pulsar in this *Fermi* LAT source. The 2.379-ms candidate was finally confirmed with observations made at the Green Bank Telescope at 350 MHz with the Green Bank Ultimate Pulsar Processing Instrument backend[2] during a survey of *Fermi* LAT unassociated sources (see Hessels et al. 2011), and at the Arecibo telescope at 327 MHz with the Wide-band Arecibo Pulsar Processors (WAPPs; Dowd, Sisk & Hagen 2000). Substantial accelerations of the rotational period across the confirmation observations were measured, indicating that the pulsar is in a binary system.

2.2 Arecibo observations

Radio light curves of PSR J2043+1711 recorded with the Arecibo telescope are shown in Fig. 1. At 1.4 GHz, the pulsar is observed to exhibit dramatic radio flux variations, explaining the several unsuccessful attempts to confirm the pulsar at Nançay following the discovery. Even with Arecibo, it can be a difficult object: during one 30-min observation the pulsar was not visible in one of the WAPPs, centred at 1.46 GHz and with 50 MHz of bandwidth. Assuming a system temperature of $T_{\rm sys} = 25$ K, a gain of $G = 10$ K Jy^{-1}, a pulse width of 6.25 per cent (eight bins above average out of a total of 128) and a signal-to-noise ratio (S/N) smaller than 3, this corresponds to an instantaneous upper limit on the radio flux density of 5.1 μJy. However, on most occasions the pulsar is detectable with Arecibo and the high S/N light curve was recorded during a bright scintillation state. The 1.4-GHz light curve is complex, with several pulsed components. A total of four useful observations of the pulsar at 1.4 GHz have been carried out with Arecibo, between 2010 November 20 and 2011 August 24. The average radio flux density for these observations was of the order of 10 μJy.

At 327 MHz, the flux density is far more steady, and for that reason we carried out the bulk of the Arecibo timing at this frequency. The pulsar was observed 64 times between 2010 July 17 and 2011 August 25 with average integrations of 35 min using the 327-MHz receiver ($G = 11$ K Jy^{-1}, $T_{\rm sys} = 113$ K). For most observations, we use the four WAPP spectrometers in parallel. Each WAPP makes a three-level digitization of the analogue voltages over a 12.5-MHz band for both linear polarizations, autocorrelating these for a total of 512 lags. The data are then integrated for $t_{\rm s} = 64$ μs and the orthogonal polarizations added in quadrature are written to disk. Their bands are centred at 308.25, 320.75, 333.25 and 345.75 MHz, and together they cover the full 50-MHz band provided by the receiver. For all Arecibo observations, the lags were Fourier transformed to generate power spectra. These were dedispersed at the nominal DM of the pulsar and folded modulo its spin period using the PRESTO pulsar software package, generating pulse profiles that are then stored for later analysis. 10 Arecibo observations at 345 MHz were averaged to derive a radio flux density of $S_{345} = 1.2$ mJy with a standard deviation of 0.2 mJy, assuming a pulse width of 6.25 per cent.

Note that this pulse width is overestimated because of instrumental limitations: with the WAPPs, the pulses are seen with an effective width at half-maximum dt given by the sum in quadrature of the intrinsic width at half-maximum $dt_{\rm i}$, the sampling time $dt_{\rm s}$ and the dispersive smearing $dt_{\rm d}$. At an observing frequency $\nu = 0.345$ GHz, we have $dt_{\rm i} \sim 75$–80 μs (see below). The sampling time is 64 μs, and with a bandwidth of 12.5 MHz for each WAPP, and 512 spectral channels across that bandwidth, the dispersive smearing $dt_{\rm d}$ (see e.g. equation 5.2 of Lorimer & Kramer 2005) is calculated to be ∼120 μs. Therefore, we have an effective width of ∼156 μs, twice as much as the intrinsic pulse width. The intrinsic pulse profile was determined using the Pulsar Machine II backend (Karuppusamy, Stappers & van Straten 2008) at the Westerbork Synthesis Radio Telescope (WSRT), in the Netherlands, which is capable of coherent dedispersion for a total bandwidth of 80 MHz centred at 345 MHz (see Fig. 1).

2.3 Timing analysis

The best detections of the pulsar at each instrument and frequency were used to derive 'standard' pulse profiles. For the dominant Arecibo 327 MHz data set, we made one time of arrival (TOA) per WAPP for every 500 s of observations on average, by cross-correlating the pulse profiles with the standard profiles in the Fourier domain (Taylor 1992). We also extracted 32 TOAs from the 1.4 GHz Arecibo observations. This resulted in a total of 1029 Arecibo TOAs. In addition, 18 NRT TOAs have been recorded at

[2] https://safe.nrao.edu/wiki/bin/view/CICADA/NGNPP

Downloaded from http://mnras.oxfordjournals.org/ at NASA Goddard Space Flight Ctr on July 14, 2014

1.4 and 1.6 GHz from 2010 August 16 to 2011 August 15 using the procedure and instrumentation described in Cognard et al. (2011). Six TOAs were recorded at 345 MHz with the WSRT between 2011 March 18 and 2011 August 20. Finally, gamma-ray pulsations from PSR J2043+1711 were detected in the *Fermi* LAT data after the first months of radio timing following the discovery (see Section 2.4), which allowed us to measure TOAs using the maximum-likelihood techniques described in Ray et al. (2011) and recover phase coherence across the entire *Fermi* LAT data set. A total of 13 gamma-ray TOAs with average uncertainty 25.3 μs and corresponding to at least 3σ detections were extracted between 2008 September 12 and 2011 June 10 by selecting photons with energies greater than 0.5 GeV and with reconstructed directions found within 1° of the pulsar.

We carried out subsequent TOA analyses using the TEMPO2 software package (Hobbs, Edwards & Manchester 2006). For the conversion of Terrestrial Time TOAs to Coordinated Barycentric Time (TCB), we used the DE/LE 421 Solar system ephemeris (Folkner, Williams & Boggs 2009). The differences between observed and predicted barycentric TOAs (the timing residuals) were weighted in the fit according to the estimated uncertainty of each TOA. The resulting timing parameters and their 1σ uncertainties are presented in Table 1. The orbit of PSR J2043+1711 has very low eccentricity, therefore we used the 'ELL1H' orbital model (Lange et al. 2001; Freire & Wex 2010) to model it. This yields Keplerian (semimajor axis of the pulsar orbit projected along the line of sight, x, orbital period P_b, epoch of ascending node T_0, eccentricity e and longitude of periastron, ω) and post-Keplerian (orthometric amplitude h_3 and orthometric ratio ς) parameters that are weakly correlated with each other.

This ephemeris describes the TOAs well, with a reduced χ^2 of 2.1 for 1044 degrees of freedom. In order to estimate the timing parameters with realistic uncertainties, we adjusted the uncertainty estimates of each individual timing data set using EFAC parameters so that $\chi^2/n_{\rm free}$ is equal to 1 in every case. The uncertainties quoted in Table 1 were derived in this fit by TEMPO2, except where stated otherwise. The 1029 Arecibo TOAs have a post-fit rms uncertainty of 2.13 μs, despite the aforementioned smearing caused by the instrumentation used to date. For this reason, PSR J2043+1711 has been added to the International Pulsar Timing Array (Hobbs et al. 2010).

There is clearly scope for further improvement in the timing precision of this object, given the fact that the pulse width measured with the WAPPs is twice as wide as the intrinsic pulse width. This implies that, with a broad-band coherent dedispersion instrument working at Arecibo, the measured peak flux density should be about twice as large and the rise time about half as long, implying about four times the current timing precision.

Note that the DM value and its uncertainty were measured independently from the analysis described here. To measure the DM, we built a data set of 308.25, 320.75, 333.25 and 345.75 MHz Arecibo TOAs by cross-correlating the individual pulse profiles with a single standard profile, to prevent any phase shifts caused by the usage of different template profiles. This data set was then fitted for the DM, yielding the best-fitting value and corresponding uncertainty listed in Table 1.

Because the radio timing data cover only slightly more than a year, no proper motion could be measured with these data alone. However, with the gamma-ray TOAs covering approximately 3 years, we could measure a significant proper motion (see Table 1). It is clear that the proper motion measurement depends strongly on the gamma-ray timing. We therefore checked the proper motion values and their associated uncertainties by studying the influence of the LAT timing on the measurement. We first repeated the analysis described above using different numbers of gamma-ray TOAs, from 5 to 25 with a step of 1. This yielded average proper motion values that are consistent with those listed in Table 1, within standard deviations on $\mu_\alpha \cos(\delta)$ and μ_δ of 0.1 and 0.4 mas yr^{-1}, respectively. Also, we made 1000 realizations of a Monte Carlo simulation in which gamma-ray TOAs were generated based on the timing solution given in Table 1, and were then perturbed so that the residuals have the same rms as those of the actual gamma-ray TOAs (∼30 μs). The uncertainties were finally shuffled from the actual gamma-ray TOAs. Again, this yielded average $\mu_\alpha \cos(\delta)$ and μ_δ values that are compatible with the values reported here, within standard deviations of 0.6 and 0.7 mas yr^{-1}, respectively. Combining the standard deviations obtained from these two studies, we estimate that the gamma-ray TOAs introduce systematic uncertainties on $\mu_\alpha \cos(\delta)$ and μ_δ of approximately 1 mas yr^{-1}.

2.4 Gamma-ray analysis

The analysis of the LAT data was done using the *Fermi* Science Tools[3] (STs) v9r23p1. We selected events recorded between 2008 August 4 and 2011 July 21, with reconstructed directions within a 20° × 20° region centred on the pulsar position, energies between 0.1 and 100 GeV, and zenith angles below 100°. We further selected 'Source' class events of the P7_V6 instrument response functions (IRFs), and rejected times when the rocking angle of the telescope exceeded 52° and when the Earth's limb infringed upon the region of interest (ROI). The gamma-ray events were phase folded using the *Fermi* plug-in distributed with TEMPO2 (Ray et al. 2011) and the ephemeris given in Table 1.

To measure the spectral properties of the pulsar, we fitted sources in the ROI using a binned maximum-likelihood method, using the PYLIKELIHOOD module provided with the STs. The spectral parameters of the 54 2FGL catalogue sources within 20° of the pulsar were included in the model. PSR J2043+1711 and the eight other pulsars in the field of view were modelled as exponentially cut-off power laws of the form

$$\frac{{\rm d}N}{{\rm d}E} = N_0 \left(\frac{E}{1\,{\rm GeV}}\right)^{-\Gamma} \exp\left[-\left(\frac{E}{E_{\rm c}}\right)\right]. \quad (1)$$

In this equation, N_0 denotes a normalization factor, Γ is the photon index and $E_{\rm c}$ is the cut-off energy of the spectrum. The extragalactic diffuse emission and the residual instrument background were modelled jointly using the *iso_p7v6source* template, while the Galactic diffuse emission was modelled using the *gal_2yearp7v6_v0* mapcube. The spectral parameters of the 12 sources within 10° of PSR J2043+1711 were left free in the fit, as were the normalization factors for the diffuse components. The nearest source in the catalogue, 2FGL J2031.0+1938, is located ∼3°.7 away and its gamma-ray energy flux above 0.1 GeV is about three times smaller than that of PSR J2043+1711. The measurement of spectral properties for the latter object is therefore weakly affected by the neighbouring sources. The gamma-ray spectral energy distribution of PSR J2043+1711 for an exponentially cut-off power law is shown in Fig. 2. The best-fitting spectral parameters, as well as the integrated photon and energy fluxes above 0.1 GeV, are listed in Table 1. With the measured energy flux F_γ, we derived the gamma-ray luminosity $L_\gamma = 4\pi f_\Omega F_\gamma d^2$ and efficiency of conversion of spin-down power into gamma-ray emission, $\eta = L_\gamma/\dot{E}$,

[3] http://fermi.gsfc.nasa.gov/ssc/data/analysis/scitools/overview.html

© 2012 The Authors, MNRAS **422,** 1294–1305
Monthly Notices of the Royal Astronomical Society © 2012 RAS

Downloaded from http://mnras.oxfordjournals.org/ at NASA Goddard Space Flight Ctr on July 14, 2014

Table 1. Measured and derived parameters for PSR J2043+1711. Numbers in parentheses are the nominal 1σ TEMPO2 uncertainties in the least-significant digits quoted. The distance was estimated using the NE2001 model of Galactic free electron density (Cordes & Lazio 2002). We assumed an uncertainty on this distance estimate of 20 per cent. Using this distance estimate and the measured proper motion, $\mu_{\rm T}$, we calculated the period derivative corrected for the Shklovskii effect (Shklovskii 1970), $\dot{P}_{\rm corr}$, and used that value to derive $\dot{E}$, $B_{\rm s}$ and $B_{\rm LC}$. Note that $\dot{E}$, $B_{\rm s}$, $B_{\rm LC}$ and η were calculated assuming a moment of inertia I of 10^{45} g cm^2. For proper motion parameters and for the total proper motion, the first quoted uncertainties are the 1σ statistical uncertainties from TEMPO2 and the second ones are systematic (see Section 2.3 for details on the calculation of the systematic uncertainties). For gamma-ray parameters, the first quoted uncertainties are statistical and the second are systematic, and correspond to the differences observed when doing the spectral analyses with the P6_V3 IRFs and associated diffuse models.

RA (J2000)	$20^{\rm h}43^{\rm m}20\overset{\rm s}{.}883\,09(5)$
Dec. (J2000)	$+17^\circ 11' 28\overset{''}{.}948(1)$
Rotational period, P (ms)	2.379 878 960 26(4)
Apparent period derivative, $\dot{P}$ (10^{-21})	5.24(2)
Proper motion in right ascension, $\mu_\alpha \cos(\delta)$ (mas yr^{-1})	$-7 \pm 1 \pm 1$
Proper motion in declination, μ_δ (mas yr^{-1})	$-11 \pm 2 \pm 1$
Epoch of ephemeris, T_0 (MJD)	55400.00019
Dispersion measure, DM (cm^{-3} pc)	20.709 87(3)
Orbital period, $P_{\rm b}$ (d)	1.482 290 809(2)
Projected semimajor axis, x (lt s)	1.623 9614(1)
Epoch of ascending node, $T_{\rm asc}$ (MJD)	55253.8038503(6)
$\eta \equiv e\sin\omega$ (10^{-6})	−2.1(1)
$\kappa \equiv e\cos\omega$ (10^{-6})	−2.6(1)
h_3 (μs)	0.63(7)
ς (μs)	0.87(5)
Span of timing data (MJD)	54729.1–55798.2
Number of TOAs	1066
rms of TOA residuals (μs)	2.1
Solar system ephemeris model	DE421
Units	TCB
Flux density at 327 MHz, S_{327} (mJy)	1.2 ± 0.2
Derived parameters	
Orbital eccentricity, e (10^{-6})	3.4(1)
Mass function, f ($M_\odot$)	0.002 092 87(8)
Minimum companion mass, $m_{\rm c}$ ($M_\odot$)	≥0.173
Galactic longitude, l (°)	61.92
Galactic latitude, b (°)	−15.31
Distance inferred from the NE2001 model, d (kpc)	1.8 ± 0.4
Total proper motion, $\mu_{\rm T}$ (mas yr^{-1})	$13 \pm 2 \pm 1$
Shklovskii-corrected period derivative, $\dot{P}_{\rm corr}$ (10^{-21})	3.6 ± 0.5
Spin-down luminosity, $\dot{E}$ (10^{34} erg s^{-1})	1.1 ± 0.2
Surface magnetic field strength, $B_{\rm s}$ (10^7 G)	9.3 ± 0.7
Magnetic field strength at the light cylinder, $B_{\rm LC}$ (10^4 G)	6.3 ± 0.5
Light-curve parameters	
First peak position, Φ_1	0.17 ± 0.01
First peak full width at half-maximum, FWHM$_1$	0.10 ± 0.02
Second peak position, Φ_2	0.58 ± 0.01
Second peak full width at half-maximum, FWHM$_2$	0.10 ± 0.03
Radio-to-gamma-ray lag, δ	0.18 ± 0.01
Gamma-ray peak separation, Δ	0.41 ± 0.02
Gamma-ray spectral parameters	
Spectral index, Γ	$1.4 \pm 0.1 \pm 0.4$
Cut-off energy, $E_{\rm c}$ (GeV)	$3.2 \pm 0.6 \pm 1.0$
Photon flux (>0.1 GeV) (10^{-8} cm^{-2} s^{-1})	$2.8 \pm 0.3 \pm 0.9$
Energy flux (>0.1 GeV), F_γ (10^{-11} erg cm^{-2} s^{-1})	$2.8 \pm 0.2 \pm 0.3$
Luminosity, L_γ/f_Ω (10^{34} erg s^{-1})	$(1.0 \pm 0.1 \pm 0.1) \times (d/1.8\,{\rm kpc})^2$
Efficiency, η/f_Ω	$(1.0 \pm 0.1 \pm 0.1) \times (d/1.8\,{\rm kpc})^2$

assuming a geometrical correction factor f_Ω (see Watters et al. 2009, for the definition) of 1, which is typical under outer magnetospheric gamma-ray emission models (see e.g. Venter, Harding & Guillemot 2009). The best-fitting spectral parameters for the sources within 10° were compatible within statistical and systematic uncertainties with the values published in the 2FGL catalogue, with the exception of 2FGL J2035.4+1058, located 6°.5 away from PSR J2043+1711, for which our flux estimate is larger than the 2FGL flux by four standard deviations. The 2FGL source J2035.4+1058, which is associated with the blazar PKS 2032+107, is nevertheless flagged in

Downloaded from http://mnras.oxfordjournals.org/ at NASA Goddard Space Flight Ctr on July 14, 2014

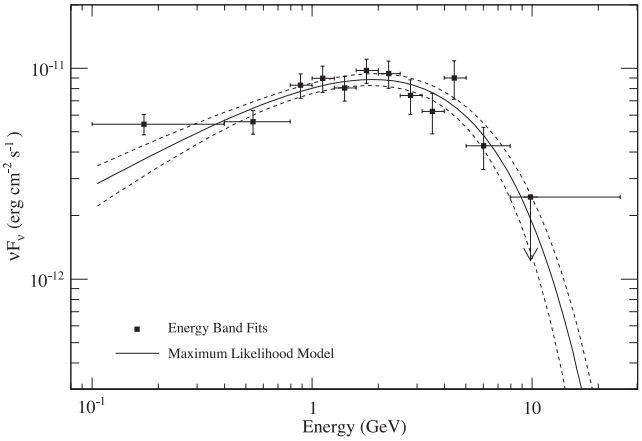

Figure 2. Phase-averaged gamma-ray energy spectrum for PSR J2043+1711. The black line shows the best-fitting model obtained by fitting the *Fermi* LAT data with a simple exponentially cut-off power-law form (see Section 2.4 for details), while dashed error lines indicate 1σ errors. Data points are derived from likelihood fits of individual, variable-width energy bands defined by the requirement that the pulsar be detected with a test statistic (see Mattox et al. 1996) of at least 50. In these bands, the pulsar is modelled with a simple power-law form. An upper limit was calculated for the last energy band as the pulsar was not detected with enough significance in that band.

the catalogue as being variable. Since the time interval considered in our analysis was longer than in the 2FGL catalogue, it is not surprising that the flux we measured differs from the 2FGL one. We checked the best-fitting spectral parameters for PSR J2043+1711 by fitting the data with the POINTLIKE likelihood analysis tool (Kerr 2011b), and found results that are consistent with those listed in Table 1 within uncertainties.

Using the full spectral model obtained with the likelihood analysis and the tool GTSRCPROB, we calculated the probabilities that each gamma-ray event originates from the pulsar. The probability-weighted gamma-ray light curve of PSR J2043+1711 above 0.1 GeV and for events found within 5° of the pulsar is shown in Fig. 1. The weighted H-test parameter (Kerr 2011a) is 433.5, corresponding to a pulsation significance of 18.5σ. The upper two phase histograms in Fig. 1 show gamma-ray light curves for events found within 0°.8 of the pulsar position, in different energy bands. The background levels in these light curves have been calculated by summing the probabilities that events have not been produced by the MSP, as described in Cognard et al. (2011) and Guillemot et al. (2012). We verified that the weighted light curve did not show indications for emission features significantly narrower than the bin width used, by analysing the same light curve with five and 10 times the number of bins, finding no statistically significant component other than those seen in Fig. 1.

We measured the phase Φ_i and full width at half-maximum ($\mathrm{FWHM_i}$) of each gamma-ray component by fitting the two peaks in the weighted light curve with Lorentzian functions. The best-fitting parameters are listed in Table 1, along with the radio-to-gamma-ray lag, $\delta = \Phi_1 - \Phi_r$, where $\Phi_r = 0.99$ is the phase of the maximum of the 345 MHz radio profile, and the separation between the two gamma-ray peaks, $\Delta = \Phi_2 - \Phi_1$.

The gamma-ray light-curve shape of PSR J2043+1711 is similar to those of other gamma-ray MSPs (see e.g. Abdo et al. 2009; Cognard et al. 2011), suggesting that the gamma-ray emission is produced at high altitudes in their magnetospheres (Venter et al. 2009). Likewise, the spectral properties of the MSP are similar to those of other gamma-ray pulsars (Abdo et al. 2010c). The large efficiency $\eta \sim 100$ per cent indicates that the distance is very likely overestimated by the NE2001 model. In Section 3, we, however, discuss the possibility to use this large efficiency value to constrain the moment of inertia of the star, if the actual pulsar distance is close to the DM distance.

2.5 X-ray analysis

On 2010 May 3, the *Fermi* LAT unassociated source 1FGL J2043.2+1709 was observed by the *Suzaku* X-ray observatory for 18 ks, as part of an unassociated sources observation campaign. A description of this campaign and the data reduction, as well as an X-ray image of the field of view around 1FGL J2043.2+1709 as seen with *Suzaku*, can be found in Takahashi et al. (2012).

No significant X-ray source can be seen at the position of PSR J2043+1711. Assuming a power-law model with a photon index of 2, the X-ray upper limit for PSR J2043+1711 between 0.5 and 8 keV is calculated to be $\sim 4.7 \times 10^{-14}$ erg cm^{-2} s^{-1} (90 per cent confidence).

We also checked the available *Swift* X-ray Telescope observations of PSR J2043+1711, and found two, totalling ~10.5 ks of data. No X-ray sources were detected within 2 arcmin of the pulsar position, thus confirming the *Suzaku* results.

3 DISCUSSION

3.1 Light curve modelling

We have fitted the radio and gamma-ray light curves of PSR J2043+1711 to geometric simulations (assuming the vacuum retarded dipole magnetic field geometry of Deutsch 1955) using a maximum-likelihood technique. The gamma-ray light curves were fitted with the two-pole caustic (TPC; Dyks & Rudak 2003) and outer gap (OG; Cheng et al. 1986) models. For our purposes, the TPC model is taken to be a geometric realization of the slot-gap model (Muslimov & Harding 2004). The radio light curves were fitted with a hollow-cone beam, core beam and cone plus core beam models following Story, Gonthier & Harding (2007).

The gamma-ray light curve (30 bins per rotation) used for the fits was constructed using all events from the data described in Section 2.4 with reconstructed directions within 0°.8 of the pulsar radio position. Additionally, we used either the 1.4 GHz or 345 MHz radio profile (also in 30 bins) but report only results from fits with the former as the latter profile is known to be too wide; however, fits using the 345-MHz profile were used in estimating systematic biases in our procedure as discussed below.

We have used simulations with the same parameters ($P = 2.5$ ms) as those in Cognard et al. (2011) except that we have a resolution of 2.5 per cent of the polar cap opening angle ($\theta_{\mathrm{PC}} \sim \sqrt{2\pi R_{\mathrm{NS}}/Pc}$) in gap width. We scanned over the parameter phase space in order to find the best fit for each model as given in Table 2.

To account for the fact that these models are relatively simple and the likelihood surfaces can be steep around maxima, implying unrealistically small uncertainties, we have rescaled the likelihood differences by $n_{\mathrm{free}}/\{2[-\ln(\mathcal{L}_{\max})]\}$, where $\mathcal{L}_{\max}$ is the maximum-likelihood value and n_{free} is the degrees of freedom for the given fit. Assuming the log-likelihood differences follow a χ^2 distribution, this results in the best fit corresponding to a reduced $\chi^2 = 1$. The best-fitting uncertainties given in Table 2 are 68 per cent confidence level. The two widths reported are for the accelerating (w_{acc}) and emitting (w_{em}) gaps; these are the same for the TPC model.

Downloaded from http://mnras.oxfordjournals.org/ at NASA Goddard Space Flight Ctr on July 14, 2014

Table 2. Best-fitting parameters from light-curve modelling (see Section 3.1). For the gap width parameters, the maximum size is 0.10. Values of 0.0 are unphysical and should be taken to mean that the best-fitting width is less than our resolution of 0.025. For the OG models, the width of the emitting gap is constrained to be no more than one-half the accelerating gap size.

Gamma-ray model	Radio model	α (°)	ζ (°)	$w_{\rm acc}(\theta_{\rm PC})$	$w_{\rm em}(\theta_{\rm PC})$	$-\ln(\mathcal{L})$	$n_{\rm free}$	f_Ω
TPC	Hollow cone	52^{+5}_{-6}	76^{+4}_{-3}	$0.10^{+0.025}_{-0.075}$	–	142.2	54	$0.81^{+0.06}_{-0.09}$
	Core only	49^{+12}_{-7}	78^{+2}_{-7}	$0.10^{+0}_{-0.05}$	–	138.3	54	$0.78^{+0.17}_{-0.07}$
	Core + cone	50^{+5}_{-8}	77^{+3}_{-3}	$0.10^{+0}_{-0.05}$	–	136.3	53	$0.78^{+0.09}_{-0.07}$
OG	Hollow cone	56^{+2}_{-14}	79 ± 1	$0.0^{+0.075}_{-0}$	$0.0^{+0.025}_{-0}$	185.3	53	$0.92^{+0.01}_{-0.26}$
	Core only	45^{+9}_{-3}	78^{+2}_{-1}	$0.0^{+0.025}_{-0}$	$0.0^{+0.025}_{-0}$	180.6	53	$0.79^{+0.13}_{-0.05}$
	Core + cone	45^{+12}_{-3}	78^{+2}_{-1}	$0.0^{+0.025}_{-0}$	$0.0^{+0.025}_{-0}$	179.1	52	$0.79^{+0.15}_{-0.05}$

Our models are relatively simple and, in the case of the radio profiles, do not contain as many components as are implied by the data. Additionally, the geometry used for the magnetic field cannot be correct as the magnetosphere will, to some extent, be filled with charges (Goldreich & Julian 1969) which will distort the gap geometry. Therefore, we have attempted to estimate systematic biases in the best-fitting geometries reported in Table 2. To do this, we refit the data while varying the radio uncertainty by a factor of 2, varying the gamma-ray background estimate by 5 per cent, using the 1.4 GHz radio light curve in 60 bins, and performing fits with gamma-ray light curves corresponding to the energy ranges 0.1–1 and ≥1 GeV. None of these changes strongly affected the gap width parameters. Changes in geometry were typically $\lesssim 8°$; however, the OG best-fitting geometry changed by 25°–40° in one parameter for both the core and cone beam fits when the radio uncertainty was doubled and when fitting only the 0.1–1 GeV gamma-ray light curve.

The data and best-fitting model light curves are shown in Fig. 3 using the 1.4 GHz radio profile and the hollow-cone beam model. While the likelihood formally favours the TPC model, both gamma-ray models reproduce the qualitative features of the observed gamma-ray light curve (gamma-ray peak separation and bridge emission) well, and the radio model is not optimal. The OG model therefore cannot be ruled out. Fits with both the TPC and OG model do find solutions with ζ near 80° which is to be expected if the spin and orbital axes have (nearly) aligned over time.

It should be noted that the likelihood favours the core beam model in all cases. Nevertheless, under these fits we obtain impact parameters ($\beta \equiv \zeta - \alpha$) of the order of 20° which would imply a very faint radio flux for a beam falling off as a Gaussian away from the magnetic axis. Such solutions thus seem less likely. Note, however, that no polarimetric data exist for this MSP to conclusively confirm or rule out the presence of a core beam.

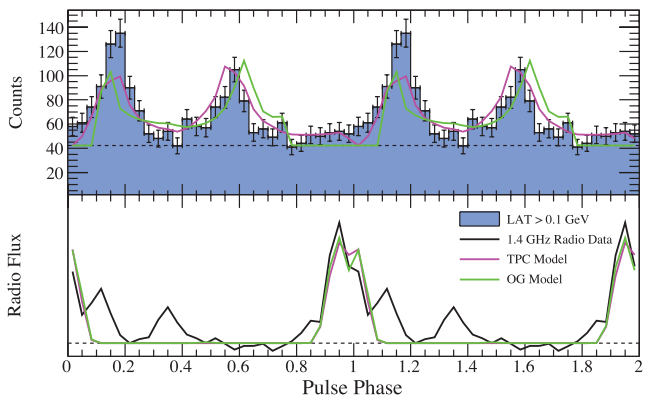

Figure 3. Data and best-fitting light curves using the gamma-ray data described in Section 3.1 (top) and the 1.4 GHz radio profile (bottom). Models corresponding to the TPC fit are shown as dot–dashed lines (solid pink lines online) and for the OG fit as dashed lines (solid green lines online).

From our models, we have estimated f_Ω (described in Section 2.4) for each model and provide estimated uncertainties (see Table 2). In all cases, the predicted f_Ω is less than 1, although relatively close. This leads to corrected gamma-ray efficiencies of $\eta = (0.8 \pm 0.1 \pm 0.1) \times (d/1.8\,{\rm kpc})^2$ for the TPC model and $\eta = \left(0.9^{+0.1+0.1}_{-0.3-0.3}\right) \times (d/1.8\,{\rm kpc})^2$ for the OG model.

3.2 Component masses

From the projected semimajor axis x and the orbital period $P_{\rm b}$, we calculate the mass function $f(m_{\rm p}, m_{\rm c}) = (m_{\rm c} \sin i)^3/(m_{\rm p} + m_{\rm c})^2 = (4\pi^2 c^3 x^3)/(G\,{\rm M}_\odot P_{\rm b}^2) \sim 2.1 \times 10^{-3}\,{\rm M}_\odot$, where $m_{\rm p}$, $m_{\rm c}$ and i are the pulsar mass, the companion mass and the orbital inclination. Assuming a pulsar mass $m_{\rm p}$ of 1.4 $\rm M_\odot$, we derive a minimum companion mass of $m_{\rm c} > 0.173\,{\rm M}_\odot$. The mass of the companion could be significantly higher for much lower orbital inclinations. However, that possibility can be excluded by our detection of relativistic time delays in the TOAs caused by space–time curvature in the vicinity of the companion star, commonly known as the Shapiro delay (Shapiro 1964); these are displayed in Fig. 4. This detection has high significance: the orthometric amplitude (h_3) measurement is nine times larger than the 1σ uncertainty. This detection implies that the orbital inclination must be high. The constraints on $m_{\rm c}$, $m_{\rm p}$ and $\sin i$ introduced by our detection of the Shapiro delay are depicted in Fig. 5. The mass function and range of companion mass values suggest that the companion star is likely to be an He-type white dwarf (WD).

The second Shapiro delay parameter, the orthometric ratio (ς), is not yet precise enough to determine astrophysically meaningful values for $m_{\rm c}$, $m_{\rm p}$ and $\sin i$. We can, nevertheless, make an estimate of $m_{\rm p}$ if we assume that the Tauris & Savonije (1999) relation between $m_{\rm c}$ and $P_{\rm b}$ applies, as it does for all known MSP/He-type WD systems with precisely measured masses (see e.g. fig. 2 of van Kerkwijk et al. 2005). For the orbital period of PSR J2043+1711, we derive $0.20 < m_{\rm c} < 0.22\,{\rm M}_\odot$, which is very close to the best value derived from the Shapiro delay measurements as can be seen from Fig. 5. In this case, the existing constraints imply $1.7 < m_{\rm p} < 2.0\,{\rm M}_\odot$ and $i = 81.3 \pm 1.0$ degrees (that is, a nearly edge-on configuration). Thus, the mass of this pulsar appears to be located

Downloaded from http://mnras.oxfordjournals.org/ at NASA Goddard Space Flight Ctr on July 14, 2014

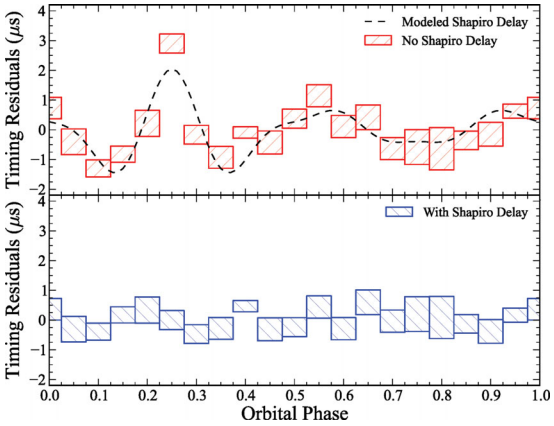

Figure 4. Arrival time residuals for the 0.3 GHz Arecibo TOAs of PSR J2043+1711, as a function of orbital phase. The timing residuals were binned in phase, with 20 bins per orbit. TOA uncertainties were taken into account when binning the timing residuals. Bottom: residuals obtained with the full timing model listed in Table 1. Top: residuals for best-fitting orbital model that does not take into account the Shapiro delay. The dashed line shows the theoretical prediction for the detectable part of the Shapiro delay (which is not absorbed by the fitting of the Keplerian parameters x and e) given by equation (19) in Freire & Wex (2010) and the h_3 and ς parameters in Table 1.

between the masses of PSR J1903+0327 (Freire et al. 2011b) and PSR J1614−2230 (Demorest et al. 2010), which define the high end of the MSP mass distribution.

3.3 Constraints on the distance and the moment of inertia

With the current set of TOAs, we were able to measure the pulsar's proper motion, finding $\mu_\alpha \cos(\delta) = -7 \pm 1\,\mathrm{mas\,yr^{-1}}$ and $\mu_\delta = -11 \pm 2\,\mathrm{mas\,yr^{-1}}$, corresponding to a total proper motion of $\mu_\mathrm{T} = 13 \pm 2\,\mathrm{mas\,yr^{-1}}$. For a distance of 1.8 kpc, this gives a transverse velocity $V_\mathrm{T} \sim 110\,\mathrm{km\,s^{-1}}$, a value that is relatively typical among Galactic disc MSPs (see e.g. Hobbs et al. 2005).

This transverse motion induces a constantly changing Doppler shift first noted by Shklovskii (1970), which makes the apparent $\dot{P}$ value greater than the intrinsic one by $\dot{P}_\mathrm{s} \sim 2.43 \times 10^{-21}\,\mathrm{s^{-1}}\,P d \mu_\mathrm{T}^2$, where P is the rotational period and d is the distance. The NE2001 model of Galactic free electron density distribution places the pulsar at 1.8 ± 0.4 kpc (Cordes & Lazio 2002). For this distance and proper motion, $\dot{P}_\mathrm{s}$ is found to represent ∼30 per cent of the measured (apparent) $\dot{P}$ value. The Shklovskii-corrected period derivative $\dot{P}_\mathrm{corr}$ and the derived pulsar properties are listed in Table 1.

An upper limit on the distance can be derived by assuming that the Shklovskii effect accounts for all of the apparent $\dot{P}$ and that the currently measured proper motion is correct. Doing so, we find $d_\mathrm{max} = 5.7$ kpc (see Fig. 6). It is clear, however, that the pulsar must

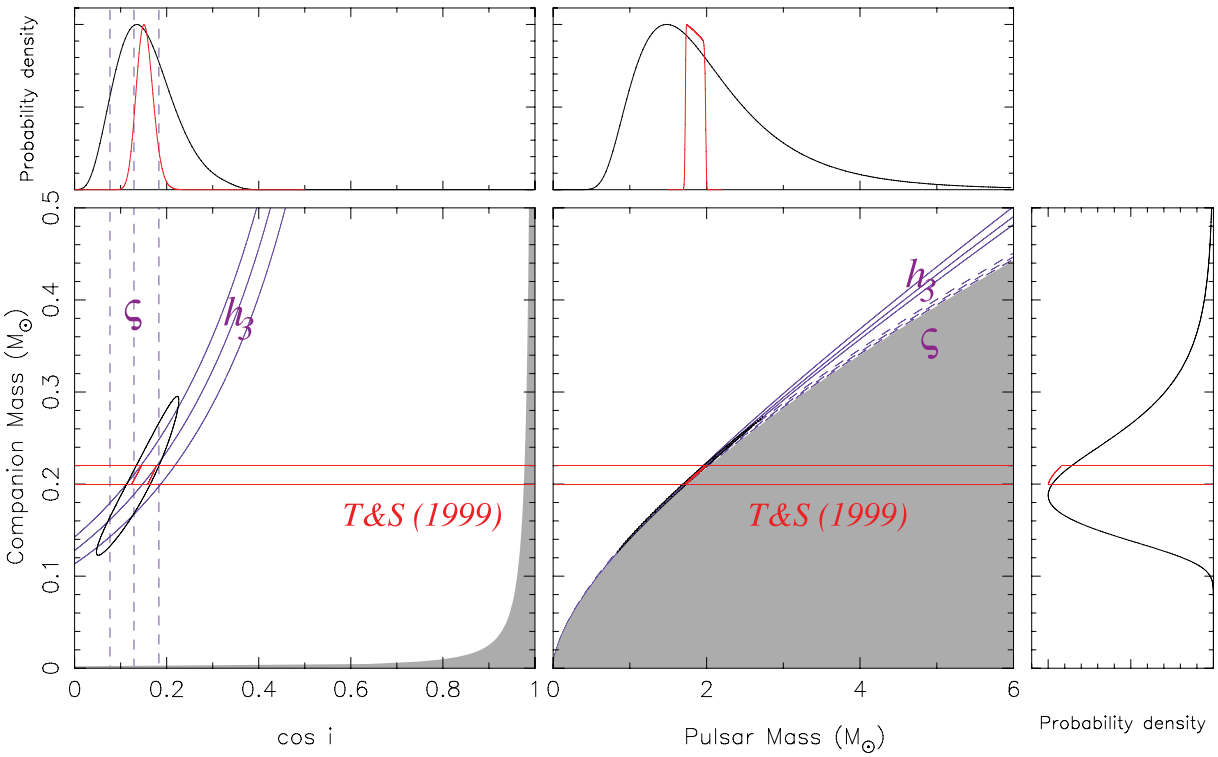

Figure 5. Constraints on some physical parameters (companion mass m_c, pulsar mass m_p and orbital inclination i) of the PSR J2043+1711 binary system. The purple curves enclose regions consistent with the nominal values and 1σ uncertainties of the Shapiro delay parameters h_3 (solid) and ς (dashed). Left: m_c–$\cos i$ plot. The grey region is excluded by the condition $m_\mathrm{p} > 0$. The black solid curve is a contour level of the 2D probability density function (PDF) that encloses 68.3 per cent of the total probability. Right: m_c–m_p plot. The grey region is excluded by the condition $\sin i \leq 1$. The black solid curve encloses 68.3 per cent of the total probability in this region of the plane, and is not a translation of the black contour curve in the left-hand plot. Top, right marginal plots: the solid black lines show the 1D probability distribution functions for $\cos i$, m_p and m_c. For all plots, the red contours represent sections of the same 2D PDF for which $0.20 < m_\mathrm{c} < 0.22\,\mathrm{M_\odot}$ according to the Tauris & Savonije (1999) model based on the orbital period measured for PSR J2043+1711.

Downloaded from http://mnras.oxfordjournals.org/ at NASA Goddard Space Flight Ctr on July 14, 2014

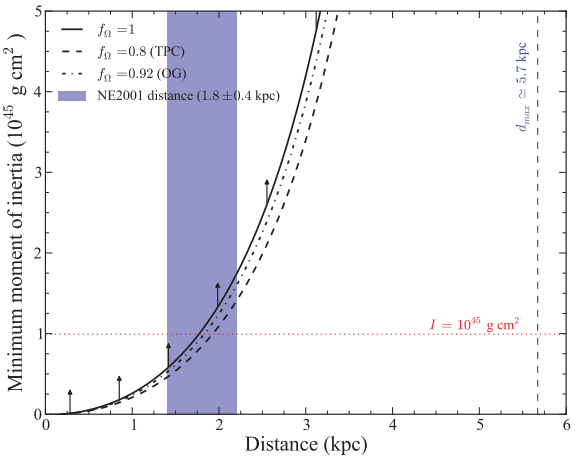

Figure 6. Upper limits on the distance as a function of the moment of inertia, imposed by the measured gamma-ray energy flux, a 100 per cent upper limit for the gamma-ray efficiency and different values for f_Ω, including best-fitting values obtained from radio and gamma-ray light-curve modelling (see Section 3.1 and Table 2). Normally I is assumed to be 10^{45} g cm^2; this would imply a maximum possible distance of about 1.8 kpc for $f_\Omega = 1$. If the distance is measured precisely, these limiting curves can be reinterpreted as lower limits on the moment of inertia. At the maximum possible distance $d_{\rm max}$ (to be refined as the measurement of the proper motion improves), the whole observed $\dot{P}_{\rm obs}$ would be due to kinematic effects, implying $\dot{P}_{\rm corr} = 0$. Therefore, for the energy loss of the pulsar $\dot{E} = 4\pi^2 I \dot{P}_{\rm corr}/P^3$ to account for the gamma-ray luminosity, I would have to be infinite.

be at a distance from the Solar system that is significantly smaller than $d_{\rm max}$. The reason for this has already been briefly mentioned in Section 2.4, namely the very high implied gamma-ray efficiency: for distances larger than 1.8 kpc, an efficiency larger than 100 per cent is required to produce the gamma-ray flux detected by the LAT.

We can derive more realistic upper limits for d based on our *Fermi* LAT measurement of the energy density G and imposing the condition $\eta < 1$. A comparison of the expressions for $\dot{E}$ and L_γ then yields the following inequality:

$$I > \frac{G f_\Omega d^2 P^3}{\pi \dot{P}_{\rm corr}(d, \mu_{\rm T})}. \quad (2)$$

For the current assumptions of $I = 10^{45}$ g cm^2 and $f_\Omega = 1$, this inequality only holds for distances smaller than 1.8 kpc (Fig. 6). For the best-fitting f_Ω factors obtained from the modelling of radio and gamma-ray light curves of PSR J2043+1711 with the TPC and OG models and with the hollow-cone beam radio model, the inequality holds for $d < 1.92$ and 1.83 kpc, respectively. The larger distances within these ranges are comparable to the distance predicted by the NE2001 model.

Improved radio timing of this pulsar might eventually allow a precise measurement of the timing parallax, and therefore of the distance d, which according to equation (2) provides a direct lower limit for I. Again, such limits are displayed in Fig. 6. As was mentioned in Section 2.4, the NE2001 model likely overestimates the distance. However, it is clear that if the model is correct or the pulsar is farther away, then its moment of inertia must be large. A high lower limit on the moment of inertia would help constrain equations of state (EoSs) for superdense matter (Worley, Krastev & Li 2008), especially if combined with a precise measurement for the mass of the pulsar, another likely consequence of the improved timing.

4 CONCLUSION AND PROSPECTS

We have reported the discovery of an MSP with the NRT at the position of an unassociated *Fermi* source, PSR J2043+1711. The pulsar is the third MSP to be discovered at Nançay in a *Fermi* source, after PSR J2017+0603 and PSR J2302+4442 (Cognard et al. 2011). The radio pulsar is found to be responsible for the gamma-ray emission observed by *Fermi*, and its properties (rotational period, spin-down luminosity, distance, gamma-ray light curve and gamma-ray spectrum) are relatively common among known gamma-ray MSPs.

Of the pulsars discovered in *Fermi* unassociated sources that have been published to date (Cognard et al. 2011; Keith et al. 2011; Ransom et al. 2011), PSR J2043+1711 and PSR J2017+0603 are the two systems with the best timing precision. This happens because they have very sharp features in their pulse profiles. Both objects are relatively faint, but they are well within the region of the sky detectable by the Arecibo 305-m telescope, which greatly compensates for the small flux density. Furthermore, both pulsars appear to be members of very stable MSP– WD binaries. For this reason, they have been included in the pulsar timing array (PTA), which is now being used in a collective effort to detect low-frequency gravitational waves (e.g. Hobbs et al. 2010).

Given this high timing precision, continued Arecibo timing might provide a precise distance measurement which, given the observed gamma-ray energy flux, would provide a lower limit for the moment of inertia of this MSP. This distance is likely to be significantly smaller than the estimate provided by the NE2001 electron model of the Galaxy, in which case the parallax should be easier to measure but the lower limit on I would not be constraining. If the distance is comparable to the DM prediction or larger, then the parallax will be more difficult to measure, but a low upper limit for the parallax would allow us to derive a high lower limit for the moment of inertia. This might constrain the EoS of neutron matter at densities above that of the atomic nucleus – some predict $I < 1.7 \times 10^{45}$ g cm^2 (Worley et al. 2008); measuring a larger lower limit for I would exclude such EoSs.

Continued timing of PSR J2043+1711 will also improve the measurement of the Shapiro delay, providing precise estimates of the masses of the components of the system. Combining this precise mass with a lower limit on the moment of inertia could provide a stringent constraint of the EoS.

ACKNOWLEDGMENTS

We would like to thank the anonymous referee for the valuable suggestions to this paper.

The *Fermi* LAT Collaboration acknowledges generous ongoing support from a number of agencies and institutes that have supported both the development and the operation of the LAT as well as scientific data analysis. These include the National Aeronautics and Space Administration and the Department of Energy in the US, the Commissariat à l'Energie Atomique and the Centre National de la Recherche Scientifique/Institut National de Physique Nucléaire et de Physique des Particules in France, the Agenzia Spaziale Italiana and the Istituto Nazionale di Fisica Nucleare in Italy, the Ministry of Education, Culture, Sports, Science and Technology (MEXT), High Energy Accelerator Research Organization (KEK) and Japan Aerospace Exploration Agency (JAXA) in Japan, and the K. A. Wallenberg Foundation, the Swedish Research Council and the Swedish National Space Board in Sweden.

Downloaded from http://mnras.oxfordjournals.org/ at NASA Goddard Space Flight Ctr on July 14, 2014

Additional support for science analysis during the operations phase is gratefully acknowledged from the Istituto Nazionale di Astrofisica in Italy and the Centre National d'Études Spatiales in France.

The Nançay Radio Observatory is operated by the Paris Observatory, associated with the French Centre National de la Recherche Scientifique (CNRS). The Arecibo Observatory is part of the National Astronomy and Ionosphere Center (NAIC), a national research centre operated by Cornell University under a cooperative agreement with the National Science Foundation. The Green Bank Telescope is operated by the National Radio Astronomy Observatory, a facility of the National Science Foundation operated under cooperative agreement by Associated Universities, Inc. The Westerbork Synthesis Radio Telescope is operated by Netherlands Foundation for Radio Astronomy, ASTRON.

REFERENCES

Abdo A. A. et al., 2009, Sci, 325, 848
Abdo A. A. et al., 2010a, ApJS, 188, 405
Abdo A. A. et al., 2010b, ApJ, 712, 957
Abdo A. A. et al., 2010c, ApJS, 187, 460
Abdo A. A. et al., 2010d, A&A, 524, A75
Abdo A. A. et al., 2012, ApJS, preprint (arXiv:1108.1435v1)
Alpar M. A., Cheng A. F., Ruderman M. A., Shaham J., 1982, Nat, 300, 728
Atwood W. B. et al., 2009, ApJ, 697, 1071
Bisnovatyi-Kogan G. S., Komberg B. V., 1974, SvA, 18, 217
Cheng K. S., Ho C., Ruderman M., 1986, ApJ, 300, 500
Cognard I., Theureau G., 2006, IAU Joint Discussion, Vol. 2, 'The Nançay Pulsar Instrumentation : The BON Coherent Dedispersor' (poster JD02-44)
Cognard I. et al., 2011, ApJ, 732, 47
Cordes J. M., Lazio T. J. W., 2002, preprint (astro-ph/0207156)
Demorest P. B., Pennucci T., Ransom S. M., Roberts M. S. E., Hessels J. W. T., 2010, Nat, 467, 1081
Deutsch A. J., 1955, Ann. Astrophys., 18, 1
Dowd A., Sisk W., Hagen J., 2000, in Kramer M., Wex N., Wielebinski R., eds, ASP Conf. Ser. Vol. 202, Pulsar Astronomy – 2000 and Beyond. Astron. Soc. Pac., San Francisco, p. 275
Dyks J., Rudak B., 2003, ApJ, 598, 1201
Folkner W. M., Williams J. G., Boggs D. H., 2009, IPN Progress Report, 42–178
Freire P. C. C., Wex N., 2010, MNRAS, 409, 199
Freire P. C. C. et al., 2011a, Sci, 334, 1107
Freire P. C. C. et al., 2011b, MNRAS, 412, 2763
Goldreich P., Julian W. H., 1969, ApJ, 157, 869
Guillemot L. et al., 2012, ApJ, 744, 33
Haslam C. G. T., Salter C. J., Stoffel H., Wilson W. E., 1982, A&AS, 47, 1
Hessels J. W. T. et al., 2011, in Burgay M., D'Amico N., Esposito P., Pellizzoni A., Possenti A., eds, AIP Conf. Ser. Vol. 1357, Radio Pulsars: an Astrophysical Key to Unlock the Secrets of the Universe. Am. Inst. Phys., New York, p. 40
Hobbs G., Lorimer D. R., Lyne A. G., Kramer M., 2005, MNRAS, 360, 974
Hobbs G. B., Edwards R. T., Manchester R. N., 2006, MNRAS, 369, 655
Hobbs G. et al., 2010, Classical Quantum Gravity, 27, 084013
Karuppusamy R., Stappers B., van Straten W., 2008, PASP, 120, 191
Keith M. J. et al., 2011, MNRAS, 414, 1292
Kerr M., 2011a, ApJ, 732, 38
Kerr M., 2011b, preprint (arXiv:1101.6072)
Kong A. K. H., Hui C. Y., Cheng K. S., 2010, ApJ, 712, L36
Kong A. K. H. et al., 2012, ApJ, 747, L3
Lange C., Camilo F., Wex N., Kramer M., Backer D. C., Lyne A. G., Doroshenko O., 2001, MNRAS, 326, 274
Lorimer D. R., Kramer M., 2005, Handbook of Pulsar Astronomy. Cambridge Univ. Press, Cambridge
Mattox J. R. et al., 1996, ApJ, 461, 396
Muslimov A. G., Harding A. K., 2004, ApJ, 606, 1143
Ransom S. M., Eikenberry S. S., Middleditch J., 2002, AJ, 124, 1788
Ransom S. M. et al., 2011, ApJ, 727, L16
Ray P. S. et al., 2011, ApJS, 194, 17
Romani R. W., Shaw M. S., 2011, ApJ, 743, L26
Saz Parkinson P. M., 2011, preprint (arXiv:1101.3096)
Shapiro I. I., 1964, Phys. Rev. Lett., 13, 789
Shklovskii I. S., 1970, SvA, 13, 562
Story S. A., Gonthier P. L., Harding A. K., 2007, ApJ, 671, 713
Takahashi Y. et al., 2012, ApJ, 747, 64
Tauris T. M., Savonije G. J., 1999, A&A, 350, 928
Taylor J. H., 1992, R. Soc. Lond. Philos. Trans. Ser. A, 341, 117
van Kerkwijk M. H., Bassa C. G., Jacoby B. A., Jonker P. G., 2005, in Rasio F. A., Stairs I. H., eds, ASP Conf. Ser. Vol. 328, Binary Radio Pulsars. Astron. Soc. Pac., San Francisco, p. 357
Venter C., Harding A. K., Guillemot L., 2009, ApJ, 707, 800
Watters K. P., Romani R. W., Weltevrede P., Johnston S., 2009, ApJ, 695, 1289
Worley A., Krastev P. G., Li B.-A., 2008, ApJ, 685, 390

APPENDIX A: RADIO SEARCH OBSERVATIONS WITH THE NANÇAY RADIO TELESCOPE

To avoid redundant observations with other instruments, and to inform the community of existing data samples, Table A1 lists all pulsar searches of *Fermi* error ellipses made with the NRT to date.

For each observation, Table A1 lists the observation time $T_{\rm obs}$, the sky temperature in the corresponding direction $T_{\rm sky}$ and the minimum detectable flux density $S_{\rm min}$. The sky temperature $T_{\rm sky}$ corresponds to the contribution from the Galactic synchrotron component, calculated by scaling the 408-MHz map of Haslam et al. (1982) to the observing frequency of 1.4 GHz with a spectral index of −2.6. The quantity $S_{\rm min}$ was estimated using the modified radiometer equation (see e.g. Lorimer & Kramer 2005), with $G = 1.4\,{\rm K\,Jy^{-1}}$, $n_{\rm p} = 2$, $\beta = 1.05$, $T_{\rm sys} = T_{\rm rec} + T_{\rm sky}$, with $T_{\rm rec} = 35\,{\rm K}$ (note that this receiver temperature includes the 2.7 K temperature from the cosmic microwave background), $\Delta f = 128\,{\rm MHz}$, and assuming $({\rm S/N})_{\rm min} = 5$, and $W = 0.1 \times P$. Also listed in the table are telescope pointing directions and the offsets from the corresponding 2FGL sources.

For each source, Table A1 gives the semimajor axis of the 95 per cent confidence ellipse (θ_{95}), the curvature significance ('Signif_Curve'), the variability index ('Variability_Index') and the name of the identified or likely associated source ('Assoc.'), if any. Details on the determination of these parameters and on the source association procedure can be found in Abdo et al. (2012).

Of the sources observed with the NRT and for which no radio pulsations have been observed to date, the following have curvature significances above 4σ and variability indices smaller than 41.6, making them good pulsar candidates: 2FGL J0224.0+6204, J0734.6−1558, J1120.0−2204, J1311.7−3429, J1625.2−0020 and J2339.6−0532. With the exception of 2FGL J0734.6−1558, in which a gamma-ray pulsar has been discovered through blind searches of the *Fermi* LAT data (Saz Parkinson 2011), these sources remain unassociated. Multiwavelength studies might help in determining their natures. Optical and X-ray observations of 2FGL J2339.6−0532 showed that it is likely to be powered by an MSP in a black-widow system (Romani & Shaw 2011; Kong et al. 2012).

Downloaded from http://mnras.oxfordjournals.org/ at NASA Goddard Space Flight Ctr on July 14, 2014

Table A1. *Fermi* LAT sources searched for radio pulsars at the NRT. Definitions of parameters and details on the calculation of the sky temperature T_{sky} and the minimum detectable flux density S_{min} for each observation are given in the text. Note that right ascensions and declinations refer to the telescope pointing directions, and not necessarily to the locations of the *Fermi* LAT sources.

2FGL name	1FGL name	l (°)	b (°)	θ_{95} (arcmin)	Date	RA (J2000.0)	Dec. (J2000.0)	Offset (arcmin)	T_{obs} (min)	T_{sky} (K)	S_{min} (μJy)	Signif_Curve	Variability_Index	Assoc.
J0031.0+0724	J0030.7+0724	114.10	−55.11	7.2	2010-01-08	$00^h30^m45^s$	+07°22′34″	5.7	58.5	0.9	47	0.8	20.9	
J0102.7+5827	J0102.8+5827	124.42	−4.38	3.6	2009-12-17	$01^h02^m50^s$	+58°27′18″	0.8	66.0	2.0	46	3.1	119.3	TXS 0059+581
					2009-12-23	$01^h02^m50^s$	+58°27′18″	0.8	66.0	2.0	46			
					2010-01-09	$01^h02^m50^s$	+58°27′18″	0.8	66.0	2.0	46			
					2010-01-10	$01^h02^m50^s$	+58°27′18″	0.8	78.0	2.0	42			
J0118.8−2142	J0118.7−2137	173.46	−81.73	2.9	2010-04-18	$01^h18^m43^s$	−21°37′39″	5.4	57.2	0.9	48	4.1	257.2	PKS 0116−219
					2010-05-14	$01^h18^m43^s$	−21°37′39″	5.4	54.6	0.9	49			
J0124.5−0621	J0124.6−0616	145.21	−67.79	12.1	2011-03-30	$01^h24^m35^s$	−06°21′51″	0.2	29.7	0.9	66	2.7	28.8	PMN J0124−0624
					2011-04-01	$01^h24^m35^s$	−06°21′51″	0.2	39.7	0.9	58			
					2011-04-30	$01^h24^m35^s$	−06°21′51″	0.2	49.7	0.9	51			
J0127.2+0324	J0127.0+0322	140.12	−58.26	5.8	2011-03-26	$01^h27^m17^s$	+03°25′11″	0.8	51.0	0.9	51	0.1	31.9	NVSS J012713+032259
					2011-03-29	$01^h27^m17^s$	+03°25′11″	0.8	51.0	0.9	51			
					2011-05-07	$01^h27^m17^s$	+03°25′11″	0.8	52.0	0.9	50			
J0131.1+6121	J0131.2+6121	127.67	−1.15	2.5	2009-12-22	$01^h31^m17^s$	+61°21′42″	1.1	66.0	2.4	46	2.4	58.1	1RXS J013106.4+612035
					2009-12-30	$01^h31^m17^s$	+61°21′42″	1.1	58.6	2.4	49			
					2009-12-31	$01^h31^m17^s$	+61°21′42″	1.1	34.7	2.4	64			
					2010-09-25	$01^h31^m17^s$	+61°21′42″	1.1	53.0	2.4	52			
					2010-12-02	$01^h31^m08^s$	+61°20′45″	0.6	31.0	2.4	68			
J0137.7+5811	J0137.8+5814	129.02	−4.12	6.0	2010-01-12	$01^h37^m46^s$	+58°14′07″	2.2	34.7	2.0	63	0.7	15.3	1RXS J013748.0+581422
					2010-01-13	$01^h37^m46^s$	+58°14′07″	2.2	66.0	2.0	46			
					2010-01-20	$01^h37^m46^s$	+58°14′07″	2.2	32.5	2.0	65			
					2010-12-01	$01^h38^m04^s$	+58°13′12″	2.7	23.5	2.0	77			
					2010-12-14	$01^h38^m04^s$	+58°13′12″	2.7	39.7	2.0	59			
J0224.0+6204	J0224.0+6201c	133.55	1.13	3.4	2011-04-08	$02^h24^m28^s$	+62°02′59″	3.1	47.4	3.0	56	7.2	20.1	
J0250.7+5631	J0251.5+5634	138.87	−2.61	7.1	2009-12-22	$02^h50^m47^s$	+56°31′50″	0.3	60.0	2.1	48	0.6	28.0	NVSS J025047+562935
					2009-12-30	$02^h50^m47^s$	+56°31′50″	0.3	55.1	2.1	50			
					2009-12-31	$02^h50^m47^s$	+56°31′50″	0.3	32.5	2.1	66			
J0334.3−3728	J0334.4−3727	240.22	−54.36	3.1	2009-11-16	$03^h34^m32^s$	−37°27′43″	2.3	57.6	0.6	47	2.7	90.3	PMN J0334−3725
					2010-01-14	$03^h34^m32^s$	−37°27′43″	2.3	60.0	0.6	46			
J0434.1−2014	J0434.1−2018	217.85	−38.94	10.2	2009-12-15	$04^h34^m13^s$	−20°18′10″	4.0	52.2	0.7	50	1.1	42.4	TXS 0431−203
					2010-04-14	$04^h34^m13^s$	−20°18′10″	4.0	19.7	0.7	81			
					2010-04-23	$04^h34^m13^s$	−20°18′10″	4.0	13.5	0.7	98			
					2010-04-24	$04^h34^m13^s$	−20°18′10″	4.0	13.5	0.7	98			
					2011-04-05	$04^h34^m13^s$	−20°18′10″	4.0	44.7	0.7	54			
J0523.3−2530	J0523.5−2529	228.23	−29.84	4.0	2009-11-08	$05^h23^m32^s$	−25°30′26″	3.0	32.2	0.6	63	2.1	22.7	
					2009-11-17	$05^h23^m32^s$	−25°30′26″	3.0	24.7	0.6	72			
J0714.0+1933	J0714.0+1935	197.68	13.61	2.6	2009-11-06	$07^h14^m02^s$	+19°34′39″	0.8	38.5	1.2	59	5.1	313.4	MG2 J071354+1934
J0734.6−1558	J0734.7−1557	232.04	2.01	3.4	2010-09-07	$07^h34^m45^s$	−15°59′18″	1.4	66.0	1.4	45	5.9	24.5	LAT PSR J0734−1559
J0928.8−3530	J0929.0−3531	263.02	11.23	7.7	2010-02-08	$09^h28^m56^s$	−35°32′16″	2.1	23.5	1.4	76	2.8	23.2	
J1120.0−2204	J1119.9−2205	276.50	36.05	3.8	2010-01-14	$11^h19^m54^s$	−22°05′06″	1.5	44.7	0.6	54	5.5	25.9	
					2010-01-17	$11^h19^m54^s$	−22°05′06″	1.5	36.0	0.6	60			
					2010-07-18	$11^h19^m54^s$	−22°05′06″	1.5	60.0	0.6	46			
					2011-03-29	$11^h19^m58^s$	−22°05′26″	0.8	56.0	0.6	48			
					2011-03-30	$11^h19^m58^s$	−22°05′26″	0.8	57.2	0.6	47			
					2011-04-22	$11^h19^m58^s$	−22°05′26″	0.8	47.2	0.6	52			

Downloaded from http://mnras.oxfordjournals.org/ at NASA Goddard Space Flight Ctr on July 14, 2014

Table A1 – *continued*

2FGL name	1FGL name	l (°)	b (°)	θ_{95} (arcmin)	Date	RA (J2000.0)	Dec. (J2000.0)	Offset (arcmin)	T_{obs} (min)	T_{sky} (K)	S_{min} (μJy)	Signif_Curve	Variability_Index	Assoc.
J1120.4+0710	J1120.4+0710	251.53	60.61	5.3	2009-11-27	$11^h20^m30^s$	+07°10′22″	0.5	27.2	0.7	69	2.8	26.6	MG1 J112039+0704
					2009-12-03	$11^h20^m30^s$	+07°10′22″	0.5	66.0	0.7	44			
					2010-07-13	$11^h20^m30^s$	+07°10′22″	0.5	66.0	0.7	44			
					2010-07-14	$11^h20^m30^s$	+07°10′22″	0.5	66.0	0.7	44			
J1129.5+3758	J1129.3+3757	175.54	69.69	8.7	2009-11-19	$11^h29^m23^s$	+37°58′19″	1.6	55.4	0.8	49	0.4	28.3	
					2010-01-11	$11^h29^m23^s$	+37°58′19″	1.6	32.9	0.8	63			
					2010-05-10	$11^h29^m23^s$	+37°58′19″	1.6	29.7	0.8	66			
					2010-05-12	$11^h29^m23^s$	+37°58′19″	1.6	26.1	0.8	71			
					2010-07-21	$11^h29^m23^s$	+37°58′19″	1.6	39.7	0.8	57			
					2010-12-01	$11^h29^m56^s$	+37°59′05″	5.0	37.2	0.8	59			
					2010-12-12	$11^h29^m56^s$	+37°59′05″	5.0	66.0	0.8	44			
J1311.7−3429	J1311.7−3429	307.69	28.20	2.0	2010-03-30	$13^h11^m47^s$	−34°29′39″	0.4	60.0	1.5	48	6.3	19.1	
					2010-05-17	$13^h11^m47^s$	−34°29′39″	0.4	37.2	1.5	60			
					2011-05-27	$13^h11^m47^s$	−34°29′39″	0.4	37.6	1.5	60			
J1340.5−0412	J1340.5−0413	325.51	56.50	8.7	2010-03-28	$13^h40^m33^s$	−04°13′56″	1.5	60.0	0.9	47	0.3	25.0	
					2010-04-13	$13^h40^m33^s$	−04°13′56″	1.5	60.0	0.9	47			
					2010-07-21	$13^h40^m33^s$	−04°13′56″	1.5	32.2	0.9	64			
					2010-09-07	$13^h40^m33^s$	−04°13′56″	1.5	41.0	0.9	57			
					2010-09-09	$13^h40^m33^s$	−04°13′56″	1.5	41.0	0.9	57			
					2010-12-02	$13^h40^m33^s$	−04°13′56″	1.5	53.5	0.9	50			
					2010-12-04	$13^h40^m33^s$	−04°13′56″	1.5	31.0	0.9	65			
					2010-12-08	$13^h40^m33^s$	−04°13′56″	1.5	27.2	0.9	69			
					2011-02-11	$13^h40^m33^s$	−04°13′56″	1.5	52.2	0.9	50			
					2011-03-22	$13^h40^m33^s$	−04°13′56″	1.5	51.0	0.9	51			
					2011-05-09	$13^h40^m33^s$	−04°13′56″	1.5	44.7	0.9	54			
					2011-05-13	$13^h40^m33^s$	−04°13′56″	1.5	46.0	0.9	53			
J1407.4−2948	J1407.9−2928	322.01	30.22	21.1	2011-03-27	$14^h07^m25^s$	−29°48′59″	0.1	58.6	1.5	48	3.2	17.6	
					2011-03-31	$14^h07^m25^s$	−29°48′59″	0.1	55.0	1.5	50			
					2011-04-02	$14^h07^m25^s$	−29°48′59″	0.1	22.2	1.5	78			
					2011-04-27	$14^h07^m25^s$	−29°48′59″	0.1	44.7	1.5	55			
					2011-05-07	$14^h07^m25^s$	−29°48′59″	0.1	43.5	1.5	56			
					2011-05-11	$14^h07^m25^s$	−29°48′59″	0.1	66.0	1.5	45			
J1625.2−0020	J1625.3−0019	13.92	31.83	3.4	2009-11-11	$16^h25^m18^s$	−00°19′15″	1.5	54.7	1.4	50	8.3	24.6	
					2009-11-19	$16^h25^m18^s$	−00°19′15″	1.5	46.0	1.4	54			
					2010-01-12	$16^h25^m18^s$	−00°19′15″	1.5	60.0	1.4	47			
J1642.9+3949	J1642.5+3947	63.48	40.95	3.2	2009-11-04	$16^h42^m32^s$	+39°46′15″	6.3	66.0	0.9	45	1.3	111.7	3C 345
					2009-11-20	$16^h42^m32^s$	+39°46′15″	6.3	66.0	0.9	45			
J2001.1+4352	J2001.1+4351	79.06	7.12	1.2	2009-11-06	$20^h01^m11^s$	+43°52′07″	0.7	24.3	2.9	78	2.1	118.0	MAGIC J2001+435
					2009-11-09	$20^h01^m11^s$	+43°52′07″	0.7	51.0	2.9	54			
					2010-01-10	$20^h01^m11^s$	+43°52′07″	0.7	57.4	2.9	51			
J2339.6−0532	J2339.7−0531	81.36	−62.47	2.5	2009-11-21	$23^h39^m44^s$	−05°31′13″	1.9	11.9	0.8	105	5.7	15.7	
					2009-11-21	$23^h39^m44^s$	−05°31′13″	1.9	21.8	0.8	77			
					2009-11-25	$23^h39^m44^s$	−05°31′13″	1.9	46.0	0.8	53			
					2010-01-12	$23^h39^m44^s$	−05°31′13	1.9	56.0	0.8	48			

This paper has been typeset from a TEX/LATEX file prepared by the author.

© 2012 The Authors, MNRAS **422,** 1294–1305
Monthly Notices of the Royal Astronomical Society © 2012 RAS

Downloaded from http://mnras.oxfordjournals.org/ at NASA Goddard Space Flight Ctr on July 14, 2014